Beamfilling Errors in Passive Microwave Rainfall Retrievals

CHRISTIAN KUMMEROW

Laboratory for Atmospheres, Goddard Space Flight Center, Greenbelt, Maryland

(Manuscript received 16 September 1996, in final form 21 July 1997)

ABSTRACT

There are currently large numbers of rainfall retrieval algorithms based upon passive microwave radiances. Most of these algorithms are physically based in that they use explicit physical assumptions to derive relationships between brightness temperatures (Tb's) and rainfall. If these assumptions involve observable quantities, then the physical basis of the algorithms can be extended to determine fundamental uncertainties in the retrieved precipitation fields. In this paper this process begins by examining the largest uncertainty in many of the physical models—the homogeneous rainfall assumption. Four months of Tropical Oceans Global Atmosphere Coupled Ocean–Atmosphere Response Experiment shipborne radar data is used to describe the horizontal characteristics of rain. The vertical hydrometeor structures needed to simulate the upwelling Tb are taken from a dynamical cloud model. Radiative transfer computations were performed using a fully three-dimensional Monte Carlo solution in order to test all aspects of the beamfilling problem. Results show that biases as well as random errors depend upon the assumed vertical structure of hydrometeors, the manner in which inhomogeneity is modeled in the retrieval, and the manner in which the radiative transfer problem is handled. Unlike previous works, the goal of this paper is not to determine a mean beamfilling correction or a vertical hydrometeor profile that should be applied to specific retrieval algorithms. Rather, it is to explore the impact of inhomogeneous rainfall upon the predicted brightness temperatures so that these relations may eventually be used to develop a physically based error model for microwave precipitation retrievals. Because the predicted Tb's depend upon assumed cloud vertical structures, the paper offers a procedure to account for the uncertainty introduced by rainfall inhomogeneity rather than a general result. The impact of inhomogeneous rainfall upon specific algorithms must still be investigated within the context of that specific algorithm.

1. Introduction

Remote sensing techniques for rainfall can be classified broadly into empirical approaches and physically based approaches. The empirical approaches use regressions between observed radiances and ground-based measurements that are taken to constitute ''truth.'' The primary advantage of these algorithms is that they are simple to implement and understand. Errors can be quantified easily based upon the best fit between radiance observations and alleged truth. Their disadvantage is that their applicability beyond the validation site is often questionable. This is of particular concern when idiosyncrasies at the truth site are propagated to the global scale of the satellite observations. Physical retrievals differ from the empirical approaches in that the retrieved rainfall is obtained from a theoretically established relation between brightness temperature (Tb) and rain rate. Establishing these theoretical relations, however, requires that certain cloud properties (e.g., horizontal structure, vertical structure, hydrometeor shapes and sizes) be assumed with sufficient detail to allow Tb computations to be performed. The advantage of all such algorithms is that the individual assumptions can be tested more easily than the empirically derived Tb to rain-rate relations and that realistic error estimates can be established once enough is known about each assumption. Except for sampling error studies (Bell 1987; Bell et al. 1990; North et al. 1993), such models have not yet been developed.

This study presents an initial step in the development of error models by examining the effect of rainfall inhomogeneity on predicted Tb. Because of the relative difficulties associated with treating three-dimensional rainfall distributions, many physical retrieval schemes have assumed rainfall to be homogeneous across the satellite field of view (FOV). This assumption, coupled with the well-known nonlinear response of Tb to rainfall rate (e.g., Wilheit et al. 1977), leads to underestimates in the retrieved precipitation. This effect has been called the ''beamfilling'' effect. Work by Short and North (1990), using a 19-GHz emission-based retrieval scheme, suggested that this underestimate may be of the order of 2 for tropical precipitation. In that study, Short and North assumed that Tb at 19 GHz could be related to the rainfall through an analytical expression of the form

$$\mathrm{Tb} = A + B \exp(-CR), \qquad (1)$$

Corresponding author address: Mr. Christian D. Kummerow, Code 912, Laboratory for Atmospheres, NASA/Goddard Space Flight Center, Greenbelt, MD 20771.
E-mail: kummerow@audry.gsfc.nasa.gov

where the constants A, B, and C were determined by empirically fitting the above relation to the radiative transfer computations done earlier by Wilheit et al. (1977). Short and North further assumed that the actual rainfall distribution could be characterized by a gamma distribution. In that case, the ''beamfilling correction'' could be expressed analytically as a function of only the parameter C in (1), which is related to the depth of the liquid column and the scale parameter β, which is related to the width of the gamma distribution. As will be shown here, however, the results derived in that study are not universally true but depend upon the author's specific assumptions regarding the vertical profiles of precipitation as well as the distribution used to describe the rainfall variability.

While many physical retrieval algorithms have addressed the issue of how to best deal with the inhomogeneous rainfall problem (e.g., Chiu et al. 1990; Petty 1994), they have not addressed the specific problem of how observed distributions of rainfall can be used to quantify errors in a generalized retrieval algorithm. In this study, we use explicit radar-derived rainfall distributions measured during the Tropical Oceans Global Atmosphere Coupled Ocean–Atmosphere Response Experiment (TOGA COARE) to illustrate how uncertainties in the observed 2-km rainfall distributions can propagate through a retrieval algorithm. This paper, however, does not address all the problems associated with error modeling in passive microwave rainfall estimation. A number of issues are not yet dealt with. Perhaps most importantly, this paper does not address the problem of uncertain vertical hydrometeor structures. Instead, it is limited to algorithms in which the vertical structure of precipitation is uniquely defined in the theoretical model used to derive the Tb to rainfall relations and does not vary as a function of the observed Tb. Such algorithms cannot yet be dealt with. Another issue that has not yet been addressed but can easily be included in the present framework is the finest scale to which rainfall inhomogeneity must be known. This study does not consider inhomogeneities finer than 2 km because of data availability. Due to the integrated nature of radiances seen by a spaceborne radiometer, one can stipulate that finer resolution may not add much to the uncertainty. Future studies, however, are needed to quantify this assertion.

a. The cloud vertical structure

To study the effect of inhomogeneous rainfall upon modeled and observed Tb, it is necessary not only to have adequate rainfall statistics but also to generate realistic microwave brightness temperatures. The latter requires that the vertical structure of hydrometeors be specified along with atmospheric variables (pressure, temperature, and relative humidity) as well as surface properties (temperature and wind speed over oceans). Since these parameters cannot be easily derived from direct radar observations, some additional information must be introduced in order to complete the forward model. In this study, we use cloud dynamical model simulations from the Goddard Cumulus Ensemble (GCE) model to construct mean hydrometeor profiles as functions of the surface rainfall. Separate profiles are used for convective and stratiform precipitation in order to make the example as realistic as possible. The cloud model is able to prescribe all the atmospheric parameters except the surface wind field, which affects the ocean emissivity. For simplicity, wind is assumed at 6 m s^{-1} in this study.

The GCE model is based upon the original cloud model developed by a number of authors including Soong and Ogura (1973) and Tao and Soong (1986). However, many significant improvements, including the addition of long- and shortwave radiation parameterizations, have been made in the past decade that allow realistic simulations of cloud-scale processes. A review of the current model can be found in Tao and Simpson (1993). The cloud microphysics include a parameterized Kessler-type two-category liquid water scheme (cloud water and rain) and parameterized (Lin et al. 1983) three-category ice-phase schemes (cloud ice, snow, and hail/graupel). The shapes of liquid and ice are assumed to be spherical in the model. The distributions of rain, snow, and graupel (or hail) are taken to be inverse exponential with respect to the diameter D such that

$$N(D) = N_0 \exp(-\lambda D), \tag{2}$$

where $N(D)$ is the number of drops of diameter between D and $D + dD$ per unit volume, $N_{0,x}$ is the intercept parameter, and λ is the slope of the distribution given by

$$\lambda = \left(\frac{\pi \rho_x N_{0,x}}{\rho q_x}\right)^{0.25}, \tag{3}$$

where ρ_x is the density, $N_{0,x}$ is the intercept parameter, q_x is the mixing ratio for each precipitating hydrometeor species, and ρ is the density of air. The typical intercept parameters used by the GCE model for rain, snow, and graupel are 0.08, 0.04, and 0.04 cm^{-4}, respectively. The density of rain, snow, and graupel are 1, 0.1, and 0.4 g cm^{-3}, respectively. The cloud water and ice droplets are assumed monodisperse. Cloud water droplets have a diameter of 1×10^{-2} cm, while cloud ice has a diameter of 2×10^{-3} cm and a density of 0.917 g cm^{-3}. The radiative transfer computations use the same assumptions as those used in the cloud dynamical model in order to ensure consistency between microphysics and computed brightness temperatures. With the prescribed sizes and densities, emission at the observed frequencies will be dominated by the cloud and rainwater, while scattering is dominated by graupel and snow. Cloud ice, due to its small size, has little impact upon the frequencies discussed here.

A stretched vertical coordinate (height increments from 220 to 1050 m) with 31 layers is used in order to maximize the resolution of the lowest levels. The model

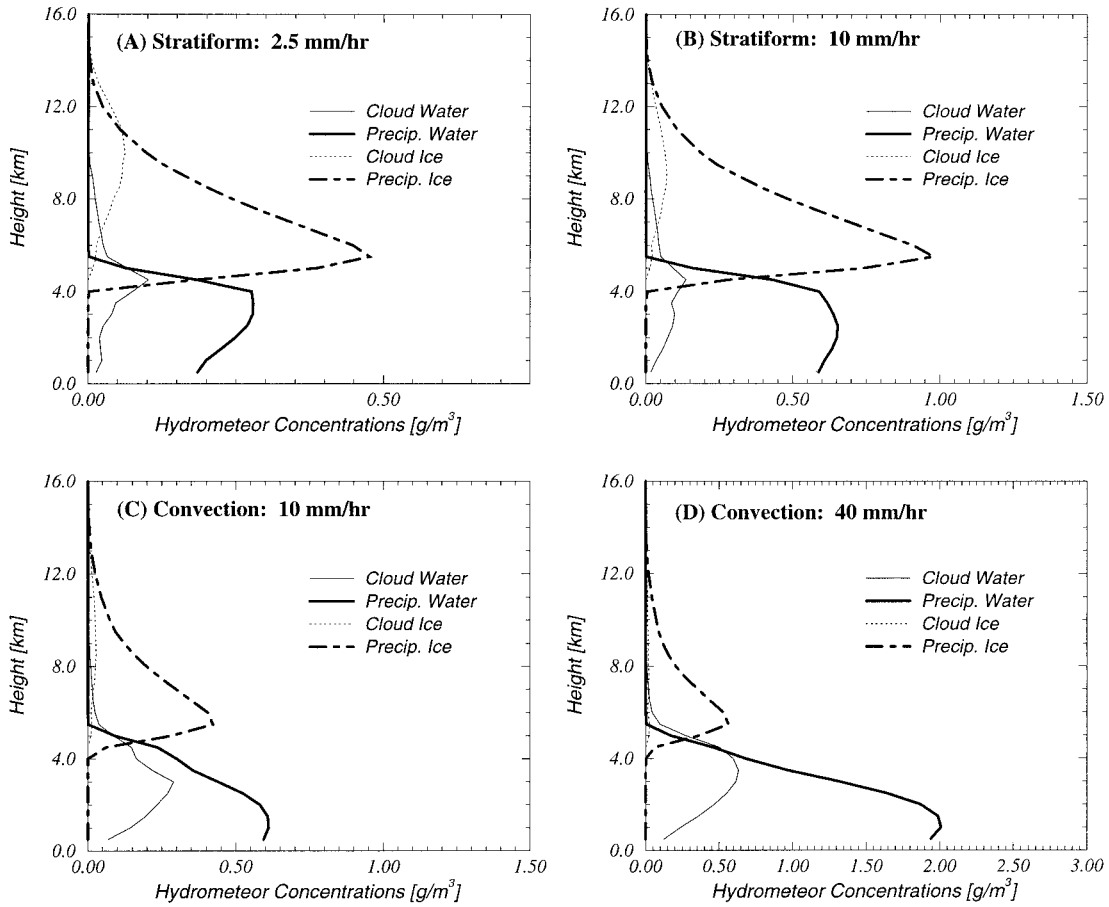

FIG. 1. Relationship for hydrometeor concentrations and surface rainfall rates for selected Goddard Cumulus Ensemble (GCE) profiles. Focusing on ''Precip. water'' and ''Precip. ice,'' the figure refers to those hydrometeors species that are large enough to precipitate out of the cloud. This includes snow, graupel, and/or hail in the case of precipitation ice.

top was 20 km. A 128 × 128 horizontal grid was used with a grid resolution of 3 km × 3 km. For this particular application, the model was initialized using the 22 February 1993 sounding from the TOGA intensive flux array (IFA). The model developed a well-defined fast moving squall line that was in good qualitative agreement with the observations.

The cloud model is used in this study to ascribe a mean vertical hydrometeor profile to surface rainfall rates determined by the TOGA radars. This was accomplished by averaging profiles within specified surface rainfall ranges. Thirty-two convective rainfall intervals ranging from 0.5 to 120 mm h^{-1} were used for convective precipitation, while 21 intervals from 0.2 to 25 mm h^{-1} were used for stratiform precipitation. The mean clear profile was also determined. Figure 1 illustrates the mean vertical profiles determined for convective and stratiform precipitation corresponding to selected rainfall rates. A number of features, such as the differences between convective and stratiform profiles for 10 mm h^{-1} rainfall rates, can be observed in this figure. Perhaps the most important feature for this study is the nonlinearity between hydrometeor concentrations shown on the horizontal axes and the surface rainfall shown at the top of each panel. While the rainfall rates quadruple from 2.5 to 10 to 40 mm h^{-1}, the hydrometeor concentration axes only double in going from panel A to panel B and panel C to panel D. This has significant implications for the brightness temperatures, which will be computed from these models. Specifically, Tb's are sensitive to the column scattering parameters, which in turn depend upon the hydrometeor content or mixing ratio within the column. They do not, as is often used colloquially, depend directly upon the surface rainfall. Thus, if the hydrometeor content M is not linearly related to the rainfall rate R, then redistributing R within a satellite FOV will not preserve the initial hydrometeor content M and will consequently lead to different brightness temperatures. For the Marshall–Palmer relations used in the cloud dynamical model as well as the radiative transfer computations, the relation between M and R is given by $R = 17.8M^{0.89}$. It is therefore immediately apparent that any attempt at redistributing surface rainfall rates within a satellite FOV will generally

not preserve the hydrometeor mass content. A more detailed analysis of this problem and its magnitude are presented in section 3.

b. Definition of terms

The overwhelming effect of rainfall inhomogeneity leads to underestimates in the retrieved rainfall. The term beamfilling correction is often used to describe the bias correction needed to compensate for this inhomogeneity. In the development of an error model, it is necessary to define inhomogeneity parameters more precisely. In this study, the spatial inhomogeneity of rainfall within the satellite FOV is designated by σ_{FOV}:

$$\sigma_{\mathrm{FOV}} = \left(\frac{1}{N_{\mathrm{FOV}} - 1} \sum_{i}^{N_{\mathrm{FOV}}} (\overline{R} - R_i)^2 \right)^{1/2}, \qquad (4)$$

where $\overline{R}$ is the FOV-averaged rainfall rate and N_{FOV} represents the number of high-resolution radar pixels in the satellite FOV. The parameter σ_{FOV} is a function of both the resolution of the radar data as well as the satellite FOV dimension. This study uses 2-km radar data in order to maximize the amount of available observations. This resolution corresponds to the analyzed TOGA rainfall maps, as well as the standard rainfall products planned for the TRMM mission (Simpson et al. 1996). Once σ_{FOV} is computed for an individual satellite FOV, it is possible to determine the mean value of σ_{FOV} as a function of either spatial or temporal domains. In this study we use the entire radar coverage area for the spatial domain and each individual intensive observation period (IOP) as the temporal domain. While it is possible to define any timescale, monthly variations seemed most suitable to this study since many products are generated at monthly timescales. Individual IOPs, which represent roughly a month of data, were therefore selected to study variations of the average σ_{FOV}. The basic parameter examined in this study is therefore $\overline{\sigma}_{\mathrm{FOV,IOP}}$, the average σ_{FOV} for each of the three IOPs over the TOGA COARE domain covered by the radars. The mean inhomogeneity, averaged over all available times, $\overline{\sigma}_{\mathrm{FOV}}$, is defined by

$$\overline{\sigma}_{\mathrm{FOV}} = \frac{1}{M} \sum_{1}^{M} \sigma_{\mathrm{FOV}}, \qquad (5)$$

where M is the total number of radar maps available. The standard deviation of the mean monthly inhomogeneity, $\overline{\sigma}_{\mathrm{FOV,IOP}}$, is defined by

$$\Gamma_{\mathrm{FOV}} = \left(\frac{1}{N_{\mathrm{IOP}} - 1} \sum_{i}^{N_{\mathrm{IOP}}} (\overline{\sigma}_{\mathrm{FOV}} - \overline{\sigma}_{\mathrm{FOV},i})^2 \right)^{1/2}, \qquad (6)$$

while the standard deviation of instantaneous inhomogeneity is given by

$$\Phi_{\mathrm{FOV}} = \left(\frac{1}{M - 1} \sum_{i}^{M} (\overline{\sigma}_{\mathrm{FOV}} - \sigma_{\mathrm{FOV}})^2 \right)^{1/2}. \qquad (7)$$

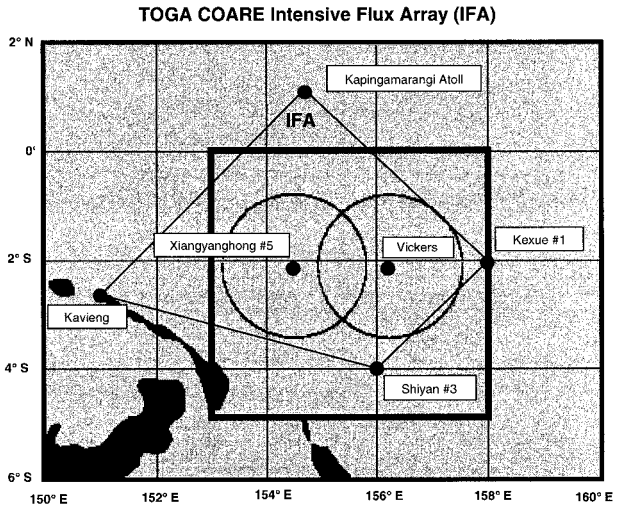

FIG. 2. Schematic diagram showing position of radar ships (*Vickers* and *Xiangyanghong #5*) within TOGA intensive flux array.

Uncertainties due to beamfilling effects, assuming no a priori knowledge of the rainfall characteristics, can thus be characterized by a mean component over the entire observation period given by $\overline{\sigma}_{\mathrm{FOV}}$; a biasing component, Γ_{FOV}, which describes the change in the mean inhomogeneity from one IOP (or month) to the next; and a random component, Φ_{FOV}, which describes the uncertainty in any given satellite FOV. The variable Γ_{FOV}, called the bias error in this study, represents the variations of σ_{FOV} on monthly scales and is thus present in monthly rainfall averages regardless of the number of rainfall observations. The instantaneous or random error represented by Φ_{FOV} will generally play only a minor role in monthly accumulations for situations with significant rainfall. For instantaneous estimates, or averages that contain only a few raining pixels, however, the effect of Φ_{FOV} may not be negligible and indeed may be larger than Γ_{FOV}.

c. The rainfall data

The radar data were collected from two 5-cm shipborne Doppler radars deployed within the IFA. Figure 2 shows the location of the radars. The *Xiangyanghong* vessel was located at 2°S, 154.5°E, while the *Vickers* was stationed at 2°S, 156°E. For about 80% of the 4-month period between 1 November 1992 and 28 February 1993, the two radars measured rainfall simultaneously. Scans were made roughly every 10 min. The derivation of rainfall rates from the observed reflectivities is described by Short et al. (1995). Rainfall results were separated into three cruises. Cruise 1 results were analyzed between 11 November and 11 December 1992. Cruise 2 analysis was from 19 December 1992 to 9 January 1993, while cruise 3 analysis was from 29 January until 19 February 1993. Cruise 1 was characterized by isolated convective rainfall events. The average rain-

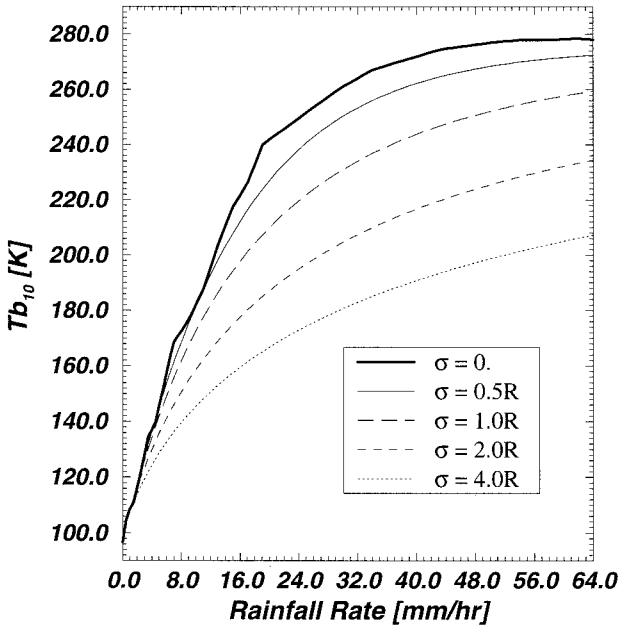

FIG. 3. The Tb to rainfall relations at 10 GHz, horizontal polarization for various values of rainfall inhomogeneity. A lognormal distribution is used.

fall was 3.00 mm day^{-1}, which was the lowest of the three cruises. Cruise 2, which had the highest mean precipitation (4.88 mm day^{-1}), was characterized by a number of large organized systems moving through the IFA area. The systems were characterized by large areas of stratiform precipitation with embedded convection. Cruise 3 had a mixture of small isolated convective systems and a few large-scale events. The average rainfall for cruise 3 was 3.43 mm day^{-1}.

2. Rainfall characteristics

The driver for beamfilling errors is, of course, the nature of the precipitation itself. While it is possible to apply an error model that makes no assumptions about the typical characteristics of rainfall, such a model would be of little or no practical use. Figure 3 illustrates this point. Shown are 10.7-GHz brightness temperatures as a function of mean footprint rainfall with different inhomogeneities. In this example, rainfall is distributed lognormally within the footprint. The different values of σ_{FOV} are indicated in the figure. As can be seen in the figure, a Tb of 240 K implies rainfall rates of approximately 12 mm h^{-1} for a homogeneous rainfall but 60 mm h^{-1} if σ_{FOV} is four times the mean rainfall in the pixel. If the characteristics of rainfall are not described, then no assumptions may be made about $\overline{\sigma}_{\text{FOV}}$, Γ_{FOV}, or Φ_{FOV}, and results on any space- and timescale will be as uncertain as any individual measurement. This condition leads to unrealistically high uncertainty estimates for monthly mean rainfall or large area averages. To reduce the uncertainty to useful levels, some properties of rainfall must be included in the analysis.

To develop a realistic error model, rainfall observations at high resolution are used to quantify the parameters $\overline{\sigma}_{\text{FOV}}$, Γ_{FOV}, and Φ_{FOV}. TOGA COARE shipborne radar data covering three periods of approximately 1 month each are used. Figures 4a–c show the relationship between the mean rainfall and the mean pixel inhomogeneity for FOV sizes of 12, 24, and 48 km, respectively. The bold solid line indicates the average inhomogeneity, $\overline{\sigma}_{\text{FOV}}$. The dark, solid error bars show the magnitude of Γ_{FOV}, while the instantaneous inhomogeneity Φ_{FOV} is represented by the thinner, dashed error bars. While the satellite FOV dimensions used in this study do not correspond directly to any particular sensor, the 48-km results represent approximately the 19-GHz resolution of the current Special Sensor Microwave/Imager (SSM/I)sensor. The 24-km resolution represents approximately the 37-GHz resolution of the SSM/I or the 19-GHz resolution of the TRMM (Tropical Rainfall Measuring Mission) Microwave Imager (TMI), as well as the Advanced Microwave Scanning Radiometer (AMSR) instrument on American Earth Observing System (EOS)-PM and the Japanese Advanced EOS (ADEOS-II) platforms. The 12-km resolutions corresponds roughly to the 85-GHz resolution of the SSM/I or the 37-GHz resolution of the TMI or AMSR instruments.

A number of results are evident from Fig. 4. The first result confirms the intuitively obvious fact that the mean inhomogeneity $\overline{\sigma}_{\text{FOV}}$, and thus the magnitude of any beamfilling correction, decreases with increasing resolution. The uncertainties, Φ_{FOV}, while appearing larger at higher spatial resolutions, are in fact smaller for a given rainfall rate. The overall effect cannot be easily characterized from this figure, however, since higher spatial resolutions also implies that higher mean rainfall rates will be encountered. A second result is that the slope of each of the three curves shown in Fig. 4 is relatively constant. This implies that offsets in the radar calibration, or somewhat uncertain *Z–R* relations used to convert radar reflectivities to rainfall, will not severely affect the results presented here. A final important feature that can be seen in Fig. 4 is that the term responsible for monthly mean biases, Γ_{FOV}, is relatively small. Assuming that enough rainfall observations are available to ignore the random component Φ_{FOV}, the relative invariance of Γ_{FOV} (despite the different rainfall characteristics in the three IOPs) will make it possible to assign useful confidence values to the retrieved monthly rainfall estimates.

The statistics presented in Fig. 4 represent approximately 3 months of tropical oceanic rainfall. Before much confidence can be vested in these numbers, however, more data from diverse regions in the Tropics should be analyzed in a similar fashion. The radars associated with the TRMM validation program should be able to provide this data. Additional data needed to add

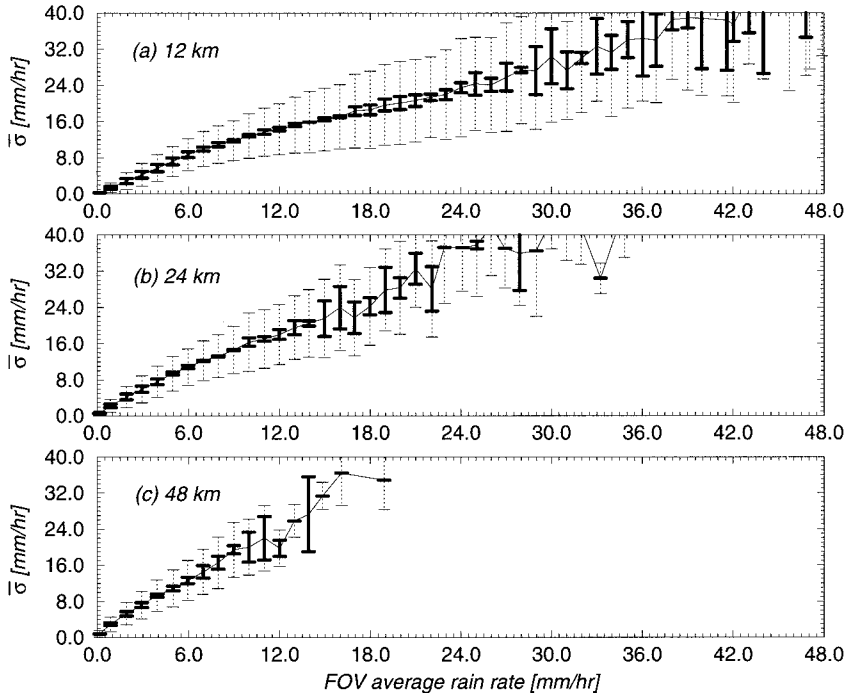

FIG. 4. Relationship between average rainfall and rainfall variability for (a) 12-, (b) 24-, and (c) 48-km satellite footprints. Thick error bars represent monthly average uncertainties, Γ_{FOV}. Dashed error bars represent random uncertainties, Φ_{FOV}.

robustness to the above example can be incorporated most easily if the mean inhomogeneity for each month, $\overline{\sigma}_{FOV,IOP}$, its square, and the number of observations in each rainfall interval are retained. Representing $\overline{\sigma}_{FOV,IOP}$, the average inhomogeneity for an individual IOP by the variable $\langle\sigma\rangle$, one can then use the relation $\Phi^2_{FOV} = \langle\sigma\rangle^2 - \langle\sigma^2\rangle$, which is valid for large N to compute the instantaneous variance of the inhomogeneity. The quantities σ_{FOV} and Γ_{FOV} can be easily computed from the previous means and number of observations. Table 1 is included in order that the current statistics may be both compared as well as expanded using other existing data sources.

3. Error model

The previous section describes a procedure for using existing and future radar data to build globally applicable statistics for $\overline{\sigma}_{FOV}$, Γ_{FOV}, and Φ_{FOV}. This section examines how rainfall inhomogeneity is treated in retrieval algorithms and the uncertainties introduced by various procedures. Three procedures that each have a significant effect upon the modeled brightness temperatures are examined. These are 1) the nonlinearities in the relationship between vertical hydrometeor contents and surface rainfall rate, 2) the errors associated with rainfall distribution functions needed to describe an inhomogeneous field in a retrieval framework, and 3) the effect of performing one-dimensional radiative transfer computations on an inherently three-dimensional problem.

a. Relations between hydrometeors and rainfall

The beamfilling effect is commonly ascribed to the nonlinear relationship between rainfall and microwave brightness temperatures in the emission portion of the spectrum. The concave nature of this relationship (see Fig. 3) causes the Tb of a homogeneous field to be higher than the corresponding Tb of an inhomogeneous field with an equivalent rainfall. Brightness temperatures, however, do not respond to the surface rainfall rate directly. Instead, they respond to the integrated hydrometeor content in the cloud. Thus, if inhomogeneous rain distributions need to be considered within satellite FOVs, it is important to consider the effect that the redistribution of surface rainfall has upon the hydrometeor concentrations. Figure 5 shows the GCE as well as the Wilheit et al. (1977) conceptual cloud model integrated liquid water content plotted against the surface rainfall. As can be seen, the integrated hydrometeor content relations have the same downward concave shape with respect to rainfall as do brightness temperature relations.

Generally speaking, retrieval algorithms that explicitly compute Tb based upon assumed cloud profiles deal with the above problem implicitly, and errors are avoided. When empirical relations between Tb and rainfall

TABLE 1. Radar statistics for 24-km FOV during three IOP periods of TOGA COARE.

	IOP-1				*IOP-2*				*IOP-3*			
(i)	N	$\langle R\rangle$	$\langle\sigma\rangle$	$\langle\sigma^2\rangle$	N	$\langle R\rangle$	$\langle\sigma\rangle$	$\langle\sigma^2\rangle$	N	$\langle R\rangle$	$\langle\sigma\rangle$	$\langle\sigma^2\rangle$
0	63 757	0.16	0.66	0.77	117 545	0.17	0.53	0.53	76 389	0.16	0.54	0.58
1	15 955	0.85	2.75	9.52	39 874	0.88	2.05	6.17	25 110	0.88	2.26	7.36
2	4396	1.92	4.97	29.31	13 023	1.93	3.80	20.22	7754	1.92	4.46	25.19
3	2044	2.93	6.73	52.31	5916	2.94	5.44	39.41	3680	2.95	6.31	47.50
4	975	3.93	8.24	75.55	3143	3.95	7.21	65.96	1982	3.95	7.95	73.88
5	591	4.94	9.70	101.19	1954	4.95	9.18	102.90	1190	4.94	9.63	104.66
6	410	5.96	11.25	134.74	1241	5.97	10.58	131.11	739	5.96	11.12	137.60
7	278	6.95	12.19	159.01	836	6.97	12.16	171.15	493	6.97	12.43	171.63
8	193	7.95	13.33	191.06	616	7.96	13.14	199.38	314	7.94	13.40	199.85
9	113	8.97	14.69	229.94	447	8.97	14.68	246.89	208	8.97	14.47	235.38
10	104	9.96	15.64	264.71	323	9.97	17.04	343.17	155	10.00	15.40	267.02
11	61	11.00	16.49	297.83	248	10.97	17.29	345.43	105	10.98	16.74	319.66
12	37	11.94	16.53	297.98	186	11.99	18.50	395.30	101	11.94	17.72	346.51
13	43	12.95	17.45	322.15	146	12.98	20.23	467.55	63	13.00	19.35	418.46
14	22	13.86	19.99	437.37	98	13.94	20.79	492.60	36	13.95	19.91	446.03
15	26	14.98	18.66	371.72	96	14.96	23.72	653.20	32	14.92	17.35	332.22
16	16	15.91	18.46	364.40	92	15.98	25.82	767.60	28	16.05	20.89	483.27
17	7	16.94	16.85	298.68	53	16.96	22.28	564.89	13	16.88	22.00	579.16
18	7	17.98	23.57	562.78	47	17.97	25.15	718.67	16	17.96	21.88	537.50
19	10	18.89	22.93	541.79	38	19.01	30.71	1030.68	14	18.99	23.64	613.72
20	0	0.00	0.00	0.00	33	19.96	29.10	948.31	12	19.96	26.18	794.99
21	0	0.00	0.00	0.00	32	21.00	33.63	1186.12	11	20.99	29.24	964.10
22	0	0.00	0.00	0.00	13	22.06	29.55	964.57	4	22.12	23.39	699.25
23	0	0.00	0.00	0.00	25	22.90	37.21	1536.72	0	0.00	0.00	0.00
24	0	0.00	0.00	0.00	16	24.10	37.18	1476.04	0	0.00	0.00	0.00
25	0	0.00	0.00	0.00	18	25.08	38.00	1585.65	5	24.98	36.96	1446.26
26	0	0.00	0.00	0.00	16	26.01	41.85	1867.96	0	0.00	0.00	0.00
27	0	0.00	0.00	0.00	13	26.92	37.03	1448.41	0	0.00	0.00	0.00
28	0	0.00	0.00	0.00	7	27.92	41.19	1747.63	6	27.85	29.68	1033.39
29	0	0.00	0.00	0.00	7	28.99	36.44	1535.43	0	0.00	0.00	0.00
30	0	0.00	0.00	0.00	5	30.01	43.40	1925.83	0	0.00	0.00	0.00
31	0	0.00	0.00	0.00	5	31.01	43.69	1995.69	0	0.00	0.00	0.00
32	0	0.00	0.00	0.00	5	31.95	41.74	1809.72	0	0.00	0.00	0.00

are employed, however, the nonlinearity between surface rainfall rate and hydrometeor concentrations can play a role and must be considered in the overall error estimate. The nonlinear relations between hydrometeor concentrations and surface rainfall all but guarantee that liquid water content in the cloud cannot be preserved if homogeneous rainfall is redistributed within a satellite FOV. Special care must therefore be taken to ensure that any empirical fit to Tb is based upon the conserved quantity, or biasing errors will be introduced into the problem. Thus, assumptions must be tracked carefully to ensure that the process of averaging or redistributing rainfall within an FOV remains consistent with the assumptions of the algorithm.

Additionally, different assumed cloud profiles will have varying degrees of nonlinearity in the hydrometeors to surface rainfall relations. This can be seen in Fig. 5, where all three clouds are somewhat different. Because the nonlinearity in this relation ultimately affects the nonlinearity of the Tb to rainfall relations, the vertical hydrometeor structures are seen to couple with the horizontal inhomogeneity problem. This implies that error models built assuming any one particular cloud will generally not be valid for different model assumptions and must instead be repeated for each specific cloud vertical structure assumed in the retrieval algorithm.

b. Rainfall distribution functions

A straightforward method to account for inhomogeneous rainfall below the satellite FOV resolution is to partition the rainfall in such a manner that the statistical properties of observed fields are reproduced. While this may be accomplished in many ways, this paper concentrates on using either lognormal or gamma distributions to describe the rainfall properties. Both the lognormal and gamma distributions have been used extensively to describe large-scale rainfall statistics. The behavior of these distributions at the relatively small scale of individual satellite FOVs, however, has received attention only recently (Kozu and Iguchi 1996). This section examines the Tb errors that result when explicit high-resolution (2 km) rain information from the TOGA radars is replaced by rainfall probability density functions (PDFs) having the same statistical properties. Specifically, this section examines the differences in the computed Tb from 1) the explicit radiative transfer computations for each satellite FOV and 2) the Tb computed from a rainfall distribution given only the mean rainfall

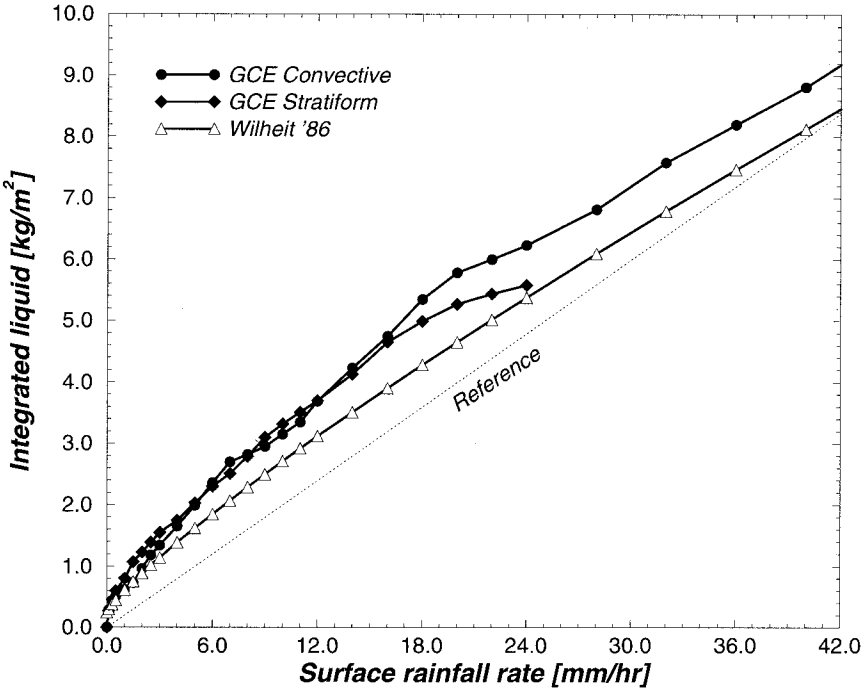

FIG. 5. Relationship between cloud integrated liquid water content and surface rainfall. A straight reference line is included to highlight nonlinear behavior.

and the variability. The explicit radiative transfer computations were performed using the radar-derived surface rainfall together with the GCE cloud structures discussed earlier. A total of 400 radar scans were utilized in these computations. The scans are spaced out at 3-h intervals so as not to introduce any potential diurnal cycle effects. Plane-parallel radiative transfer computations were performed on each 2-km pixel. The $\langle \mathrm{Tb} \rangle_{\mathrm{FOV}}$ was obtained by averaging the high-resolution Tb over the appropriate FOV size. Also computed for each satellite FOV was the mean rainfall $\langle R \rangle$ and the variability σ_{FOV}. For the case where Tb is computed from a rainfall distribution, $\langle \mathrm{Tb} \rangle_{\mathrm{FOV}}$ is computed from

$$\langle \mathrm{Tb} \rangle = \int_0^\infty \mathrm{Tb}(R) f(R)\, dr. \tag{8}$$

In the case of the lognormal distribution, $f(R)$ is given by

$$f(R) = \frac{1}{\sqrt{2\pi}\,\sigma R} \exp\left[\frac{1}{2\sigma^2}(\ln(R) - \mu)^2\right], \tag{9}$$

where $\sigma^2 = \ln(\sigma^2_{\mathrm{FOV}}/\langle R \rangle + 1)$ and $\mu = \ln(\langle R \rangle) - 0.5\sigma^2$. In the case of the gamma distribution, $f(R)$ is given by

$$f(R) = \frac{\beta^\alpha}{\Gamma(\alpha)} R^{\alpha-1} \exp\left(-\frac{R}{\beta}\right), \tag{10}$$

where $\alpha = \langle R \rangle^2/\sigma^2_{\mathrm{FOV}}$ and $\beta = \sigma^2_{\mathrm{FOV}}/\langle R \rangle$. As before, plane-parallel radiative transfer computations are performed using the GCE-derived structure appropriate for each rainfall rate in the integration defined by (8).

Figures 6 and 7 show the results of these computations for the lognormal and gamma distributions, respectively. It is apparent from Fig. 6 that the lognormal distribution does not properly capture the Tb computed explicitly. The overestimate of the Tb using the lognormal distribution behaves as if the rainfall was too homogeneous. While no proof is offered, this behavior is consistent with the fact that the lognormal distribution is known to have a long tail at high rainfall rates. This tail, while accounting for the rainfall variability, has little effect on the Tb's since these tend to saturate at relatively low rainfall rates. The gamma distribution results presented in Fig. 7 are seen to represent the explicit Tb far better than the lognormal distribution. This is probably because the gamma distribution is wider around the mean of the rainfall, with less weight given to high rainfall rates where the Tb are saturated. An important point is that in the modeling of errors, it is not the fidelity of the rainfall rate distribution that is critical, but rather the fidelity of the rainfall rate distribution convolved with the brightness temperature response.

Data were also analyzed using conditional lognormal and gamma distributions. Here, only the raining portion of the FOV is assigned to one of the above distributions. The lognormal results improved significantly by adding the rain/no-rain information. Nonetheless, the results were still not quite as good as the unconditional gamma results. The conditional gamma showed only modest improvement over the results in Fig. 7. Since using con-

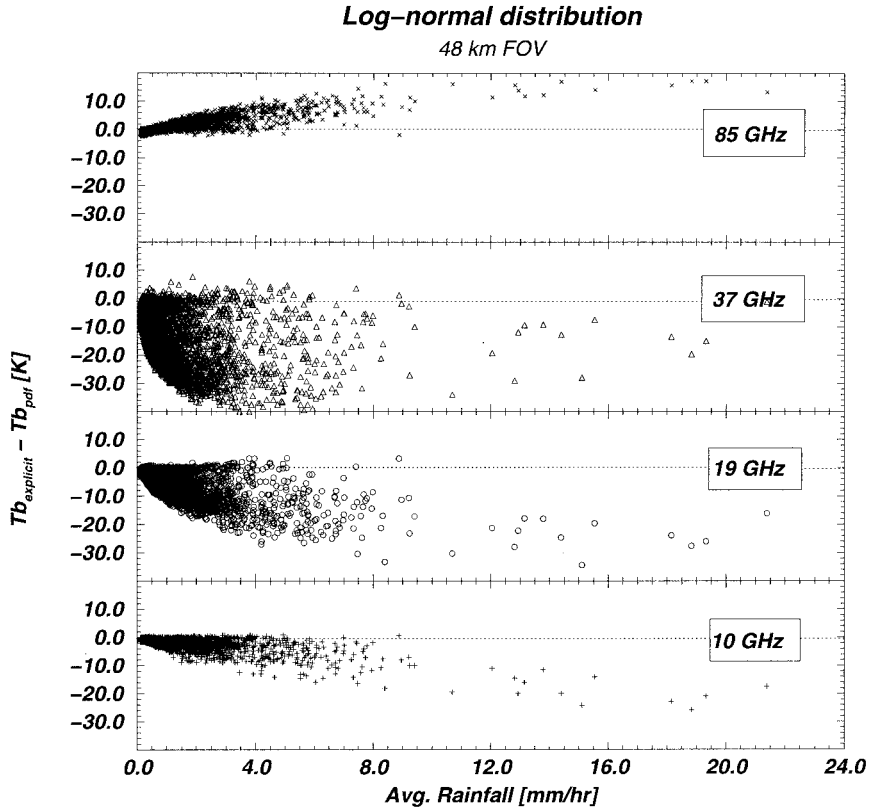

FIG. 6. FOV differences between explicitly computed Tb and those obtained assuming a lognormal distribution of equal mean and variance. Satellite FOV is 48 km.

ditional probabilities implies that an extra variable (the portion of the FOV covered by rain) be known, it was felt that any small improvement that the conditional gamma distribution could offer would be offset by the additional unknown variable. For that reason, only results from the unconditional gamma distribution are presented here. Table 2 gives the average bias and root-mean-square (rms) error that results when exact computations are replaced by a gamma distribution of equal mean rainfall and standard deviation. Results are presented for 12-, 24-, and 48-km satellite FOV in order to highlight the similarities and differences between various pixel resolutions. At 10 GHz, the biases and random errors are quite small for all three FOV sizes for rainfall rates below approximately 10 mm h^{-1}. This is probably due to the high degree of linearity in the 10-GHz Tb to rainfall relations. At 19 GHz, the higher spatial resolution is seen to have somewhat larger biases as well as larger rms errors. Comparing the 4–5-mm h^{-1} rainfall category, for instance, shows a bias of -3.1 K at 12 km, -2.3 K at 24 km, and -1.4 K at 48 km. Likewise, the random error is 4.8 K at 12 km, 4.6 K at 24 km, and 4.2 K at 48 km. Similar behavior can be observed at other rainfall rates. It thus appears that the gamma solution better captures the correct FOV properties when a greater mixture of rainfall rates is present (larger FOVs). This same behavior is seen at 37 GHz. Finally, at 85 GHz, the deviations are once again more similar across the various resolutions. This coincides with the fact that the 85-GHz Tb's are more linearly related to rainfall than either the 19- or 37-GHz channels. The positive bias in this case is related to the tendency of the Tb to decrease with increased rainfall at frequencies such as the 85 GHz, where scattering dominates the radiative signature.

As mentioned above, a successful representation of the rainfall distribution involves not only a distribution function that properly describes the rainfall but one that one that accurately represents the convolution of rainfall rates with computed Tb. Since the vertical profiles assumed by a retrieval algorithm are central in determining the Tb to rainfall relations, the above results should not be viewed as globally applicable. They are valid only for the profiles assumed in this study and must be reexamined if different assumptions are made. This is true also of the next section, which examines the effect of replacing an inherently three-dimensional radiative transfer problem with one-dimensional radiative transfer computations.

c. Three-dimensional radiative transfer effects

Up to this point, radiative transfer computations have been performed using a one-dimensional radiative trans-

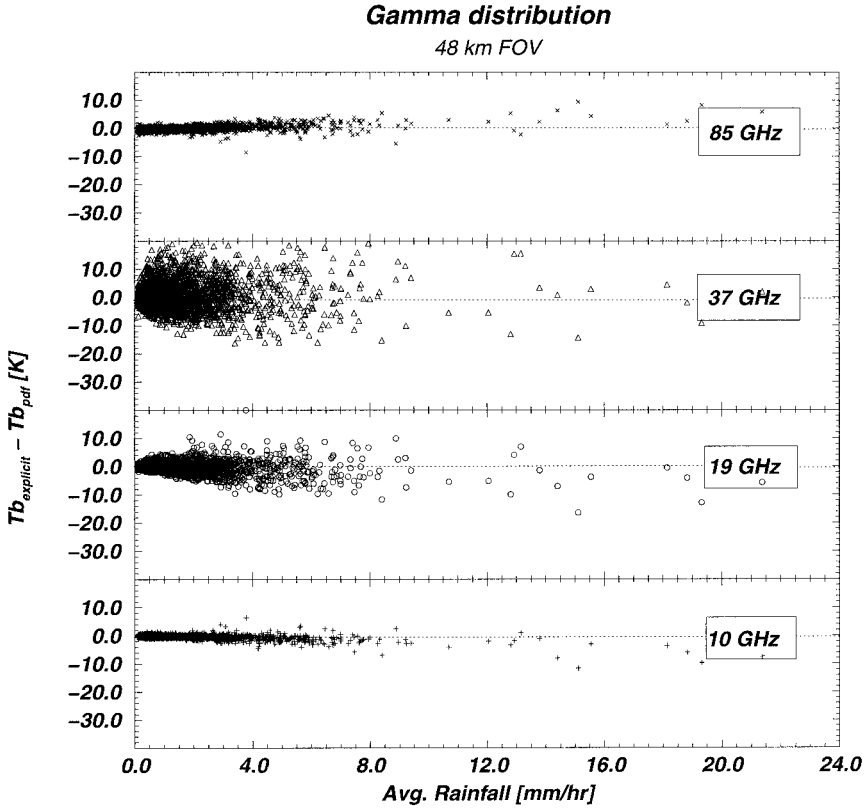

FIG. 7. FOV differences between explicitly computed Tb and those obtained assuming a gamma distribution of equal mean and variance. Satellite FOV is 48 km.

fer model. This was necessary since each of the 400 radar scans consists of 150 × 150 grid elements. At four frequencies, this constitutes 36×10^6 independent radiative transfer computations. While independent pixel computations do not require the averaging of hydrometeors, that solution does not allow radiation to pass freely from one part of the cloud to another. This section investigates biases and random errors, which are introduced when an inherently three-dimensional problem is treated with a one-dimensional solution. To investigate the three-dimensional effects, a backward Monte Carlo code developed by Roberti et al. (1994) is used to compute the full three-dimensional solution. The hydrometeor field, as before, is constructed based upon 2-km radar data in conjunction with the GCE-generated structures for appropriate rainfall rates. Because three-dimensional Monte Carlo computations are quite time consuming, it was not possible to obtain statistics from all 400 radar fields considered in the previous section. Instead, only the 49 rainiest radar scans are utilized in this portion of the study. The one-dimensional solution, although available from analytical methods, was computed using the identical Monte Carlo solution but with the radar grid elements set to 2000 km instead of 2 km. This ensures that the resulting Tb's are essentially the plane-parallel results. Any differences in the Tb's can thus be ascribed directly to the three-dimensional radiative effects instead of being sensitive to details of the radiative transfer approximation.

Before direct comparisons can be made, there is a geometrical correction that must be made. This correction is an artifact of the setup used in plane-parallel methods. Figure 8 shows a schematic of the *x*–*z* cross section of a cloud. Plane-parallel computations are typically performed on each independent column, and the resultant Tb is ascribed to the position of that column. This is true even when off-nadir viewing angles are used. In the schematic, the plane-parallel Tb from the first column is assigned to x_1 regardless of the viewing angle or the height *z* from which the signal is originating. This is necessitated by the absence of spatial information in one-dimensional models. Three-dimensional solutions treat the problem differently and assign the Tb to the point at the top of the cloud where the radiation exits. For a case where most of the radiation originates near the surface, the exit point is easily computed as $x = x_1 + z_{\text{top}} \tan\Theta$, where Θ is the satellite viewing angle. The liquid cloud shown in the schematic at the x_2 position will thus be seen at the x_2 position in plane-parallel computations but will be shifted to the x_3 position in the Monte Carlo results. Because of this behavior, one- and three-dimensional radiative transfer computations are usually shifted with respect to one another. Additionally, different channels penetrate

TABLE 2. Biases ($Tb_{explicit} - Tb_{gamma}$) and rms errors introduced by assuming rainfall to follow a gamma distribution.

		10H		19H		37H		85H	
Rain	*N*	Bias	rmse	Bias	rmse	Bias	rmse	Bias	rmse
				12-km FOV					
0–1	62 639	−0.2	0.4	−0.6	0.9	−2.2	3.3	−0.2	0.7
1–2	14 773	−0.1	0.5	−1.0	1.9	−2.9	5.8	−0.1	1.1
2–3	6579	−0.3	0.7	−1.8	2.9	−3.4	7.4	0.3	1.2
3–4	3577	−0.6	1.0	−2.6	3.9	−3.5	8.2	1.2	2.2
4–5	2226	−0.7	1.4	−3.1	4.8	−4.3	8.9	1.0	2.4
5–6	1374	−1.1	1.7	−3.7	5.7	−4.3	9.4	1.4	3.1
6–7	985	−1.3	2.1	−4.3	6.4	−4.6	9.6	2.2	3.1
7–8	664	−1.8	2.7	−5.1	7.1	−4.9	9.5	2.7	3.6
8–9	534	−1.9	2.7	−5.5	7.4	−4.9	9.5	3.0	3.8
9–10	403	−2.3	3.3	−6.2	8.1	−5.2	9.5	3.5	4.4
10–11	343	−2.3	3.6	−5.8	8.2	−4.4	9.3	3.4	4.6
11–12	289	−2.8	4.0	−6.4	8.5	−4.6	8.9	3.9	4.9
12–13	223	−3.1	4.4	−6.9	9.2	−4.9	9.0	4.2	5.4
13–14	194	−2.7	4.1	−6.1	8.4	−3.7	8.0	3.7	5.2
14–15	150	−3.2	4.7	−6.1	8.5	−3.5	7.5	3.8	5.3
15–16	123	−3.5	4.7	−6.5	8.4	−3.9	7.4	4.1	5.3
16–17	106	−4.1	5.5	−7.5	9.1	−3.8	7.0	5.1	6.2
17–18	80	−4.0	5.6	−5.8	8.2	−2.5	6.8	3.8	5.4
18–19	80	−5.1	6.5	−7.7	9.5	−5.3	9.0	4.4	5.6
19–20	71	−4.7	6.4	−6.1	9.0	−2.9	7.5	4.4	5.9
20–21	45	−4.3	5.7	−5.9	8.1	−2.4	6.1	4.2	5.7
21–22	45	−4.7	6.3	−5.8	8.0	−2.0	6.0	4.0	5.5
22–23	31	−5.3	8.0	−5.8	9.9	−3.9	8.9	4.1	6.5
23–24	32	−5.3	8.2	−5.7	8.8	−2.3	7.2	4.0	5.7
24–25	27	−5.3	6.3	−5.3	7.0	−1.2	3.7	4.0	5.3
25–26	27	−7.1	9.4	−7.0	9.6	−3.2	7.5	5.1	6.4
				24-km FOV					
0–1	20 532	−0.3	0.5	−0.6	1.0	−1.7	2.9	−0.1	0.5
1–2	4343	−0.3	0.6	−0.9	1.9	−1.3	5.5	0.1	0.8
2–3	1737	−0.4	0.8	−1.3	2.7	−1.5	6.5	0.4	1.0
3–4	877	−0.7	1.1	−1.7	3.6	−1.3	7.4	1.0	1.8
4–5	493	−0.9	1.5	−2.3	4.6	−2.2	8.6	1.1	2.0
5–6	309	−1.1	1.8	−2.7	5.2	−2.1	8.6	1.5	2.4
6–7	199	−1.5	2.2	−3.7	6.0	−2.9	9.1	2.0	2.8
7–8	134	−1.6	2.3	−4.3	6.4	−3.8	8.5	2.2	3.0
8–9	118	−1.9	3.1	−4.3	7.3	−3.2	9.5	2.6	3.8
9–10	63	−2.2	3.0	−5.3	7.3	−3.8	8.6	3.0	3.8
10–11	54	−2.9	3.9	−6.3	8.5	−5.6	10.1	3.4	4.4
11–12	51	−3.0	4.0	−7.0	8.7	−5.9	9.5	4.1	4.8
12–13	35	−2.6	4.5	−4.1	9.6	−2.3	11.5	2.6	5.3
				48-km FOV					
0–1	5608	−0.5	0.9	−0.8	1.3	−1.3	2.8	0.2	0.6
1–2	968	−0.4	0.8	−0.5	1.8	0.3	5.2	0.2	0.7
2–3	379	−0.4	0.8	−0.3	2.7	1.4	6.7	0.3	0.9
3–4	161	−0.4	1.1	−0.5	3.5	1.1	7.4	0.5	1.3
4–5	77	−0.8	1.4	−1.4	4.2	−0.1	8.0	1.0	1.6
5–6	53	−0.8	1.4	−0.2	4.2	3.7	9.6	0.7	1.7
6–7	26	−1.3	2.0	−2.6	4.9	−0.8	7.5	1.5	2.3

clouds to different depths. This shift is not constant but depends upon the radiative properties of the clouds themselves. To minimize these differences, which are due to geometrical effects, the Tb images of the Monte Carlo and plane-parallel solutions are first shifted using a mean offset for each channel. The empirically derived offset is 22 km at 10 GHz, 20 km at 19 GHz, 18 km at 37 GHz, and 14 km at 85 GHz. The physical differences between one- and three-dimensional models has been discussed in previous literature (Roberti et al. 1994; Petty 1994; Liu et al. 1996).

Results showing the mean bias (defined as $Tb_{Monte\ Carlo} - Tb_{plane\ parallel}$), as well as rms errors, are presented in Table 3. As can be seen, the biases are usually quite small. While the data are rather noisy (due to the limited number of radar scans that could be processed using the Monte Carlo code), it appears as if biases rarely exceed a few degrees kelvin. This result is consistent with earlier findings of Roberti et al. (1994) but differs from results presented by Petty (1994) or Liu et al. (1996). One explanation for the differing conclusions lies in the highly idealized, relatively small cuboidal clouds used

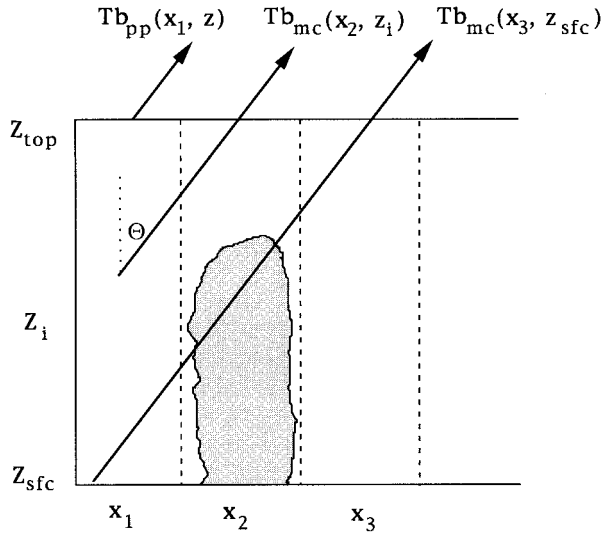

FIG. 8. Schematic cloud diagram showing the offset in Tb between one-dimensional plane parallel (Tb_{pp}) and three-dimensional Monte Carlo (Tb_{mc}) temperatures.

in both the above studies. Such idealized clouds expose large portions of their sides so the radiometer can thus significantly alter the FOV average temperatures. This effect is not nearly as pronounced in this study because the precipitating systems observed by the radar were often much larger than a single satellite FOV and had a tendency to taper off far more gradually than the idealized clouds.

Unlike biases, rms differences between one- and three-dimensional computations are quite significant, particularly at the higher-resolution FOV. The noise can be seen to decrease as footprint sizes go from 12 to 24 to 48 km. This result is consistent with earlier findings of Roberti et al. (1994), pointing toward a redistribution of radiation rather than any fundamental radiative differences in the three-dimensional solution. The rms deviations are also seen to increase with frequency up to 37 GHz but then decrease sharply for 85 GHz. This behavior is closely coupled with the nonlinearity of the Tb–rainfall relations themselves. Apparently, the high degree of nonlinearity at 37 GHz causes the largest differences when radiation is allowed to interact in three dimensions. Since the 85-GHz response is virtually linear, little or no effect is seen at that frequency.

4. An example

To illustrate how the various error sources affect a retrieval algorithm, a very simple model is used. Here, only the 19-GHz horizontal polarization is used to retrieve rainfall. As done throughout this paper, the vertical structure of the rainfall is assumed to be given by the GCE average profiles appropriate for each rainfall. Since this is an illustrative example only, no attempt is made to fit this model to actual data. The vertical structure, including the effect of cloud water and water vapor, is assumed known. The surface temperature and surface wind speed is likewise assumed known. With these assumptions in place, the forward problem is uniquely defined. The only source of uncertainty in the retrieval problem becomes the effect of rainfall inhomogeneity. The inhomogeneity is assumed to follow the statistical properties determined from the TOGA COARE radar. The example that follows is for a 24-km FOV, which is roughly the resolution of the 19-GHz channel on the TRMM and EOS–AMSR instruments.

The first step in the error model is to compute the Tb to rainfall relations, σ_{FOV}, assuming homogeneous rainfall as well as the mean inhomogeneity determined from the radar data. The mean inhomogeneity derived from the radar data is modeled using a gamma function, as discussed in section 3b. The results are shown as the thick solid line (homogeneous case) and thick dashed line (inhomogeneous case) in Fig. 9. The difference between these two curves represents the classic beamfilling adjustment. When integrated with typical rainfall distributions, the beamfilling correction factor appears very close to the value of 2 reported by Short and North (1990). This value, however, must be viewed in the context of this example since many effects such as clouds in the nonprecipitating portion of the FOV have not been considered. The latter problem is related to the vertical structure of precipitation and is not explicitly dealt with here. Once the Tb to rainfall relations for the mean inhomogeneity are established, it is straightforward to use the radar statistics to compute the expected errors in the Tb. The upper and lower limits of the bias and random inhomogeneity shown in Fig. 4 are used for these computations. The gamma distributions corresponding to the mean rainfall and inhomogeneity obtained from the radar data are used once again. Results are presented in terms of dashed lines in Fig. 9, where the long dashed lines close to the mean variance curve represent the bias component of the error and the short dashed outside lines represent the random component of the error.

The gamma distribution, as shown in section 3b, does not reproduce Tb exactly. Instead, it adds its own set of biases and random errors when compared to explicit radiative transfer computations. Furthermore, the explicit computations used to evaluate the performance of the gamma function are not free of error. Since one-dimensional independent pixel computations were used in section 3b, one must add the biases and uncertainties due to the lack of three-dimensional computations to this problem. Assuming that these errors are for the most part uncorrelated, the resulting uncertainty can be treated as the sum of the uncertainties determined in sections 3b and 3c. Adding these uncertainties to those stemming from uncertainties in the knowledge of the inhomogeneity itself (Fig. 9) leads to the overall retrieval uncertainty. This result is shown in Fig. 10. Comparing Fig. 10 with the results from Fig. 9 shows that the largest

TABLE 3. Biases ($Tb_{3D} - Tb_{1D}$) and rms errors introduced by independent pixel plane-parallel radiative approximation.

		10H		19H		37H		85H	
Rain	*N*	Bias	rmse	Bias	rmse	Bias	rmse	Bias	rmse
				12-km FOV					
0–1	26 448	0.2	2.0	0.8	3.7	1.6	7.4	0.4	1.4
1–2	866	0.3	3.2	0.5	6.2	−0.4	12.0	0.2	1.7
2–3	332	0.4	3.7	0.4	7.1	−0.6	12.0	−0.1	1.8
3–4	146	0.0	3.4	0.0	5.9	−0.9	9.6	−0.5	1.7
4–5	95	−0.5	4.0	−1.1	6.8	−1.5	11.4	−0.3	1.9
5–6	62	0.6	6.2	0.1	8.9	−0.7	11.0	−0.8	1.9
6–7	49	1.9	7.1	1.2	10.3	0.9	14.4	−0.3	2.0
7–8	38	−0.6	3.2	−2.0	6.3	−3.2	10.2	−0.5	2.0
8–9	20	0.5	4.2	−0.2	4.1	−1.1	5.7	−1.2	2.1
9–10	21	−0.9	4.2	−2.6	7.9	−3.2	11.6	−0.8	1.9
10–11	16	−0.7	2.7	−1.5	5.1	−3.6	6.2	−1.2	1.8
11–12	9	1.9	4.5	2.8	7.1	2.0	9.5	−1.4	2.0
12–13	10	−1.8	3.7	−2.2	4.6	−4.3	7.3	−0.6	1.6
13–14	14	−0.4	4.4	−2.2	8.1	−3.0	11.1	−1.0	2.1
14–15	9	−0.6	3.4	−2.8	6.5	−3.6	8.0	−0.6	2.2
15–16	6	−0.1	2.4	−2.8	3.8	−9.2	13.4	−2.1	2.3
16–17	7	0.3	1.1	−1.0	2.7	−1.9	5.0	−0.9	1.6
17–18	7	0.2	2.2	−0.8	5.2	−1.7	6.3	−1.7	2.4
				24-km FOV					
0–1	23 790	0.2	1.3	0.8	2.5	1.7	5.4	0.4	1.0
1–2	1154	0.6	2.2	1.0	4.3	1.9	7.9	0.3	1.1
2–3	385	0.6	2.4	0.4	4.5	1.2	7.8	0.0	1.0
3–4	172	0.9	3.2	0.6	4.9	1.1	7.9	0.0	1.2
4–5	132	0.7	3.2	0.2	5.1	0.1	7.3	−0.2	1.1
5–6	69	0.4	3.5	−0.7	4.7	−0.8	6.7	−0.4	1.1
6–7	45	0.0	2.2	−1.0	4.2	0.0	6.0	−0.3	1.1
7–8	41	−0.3	2.7	−1.7	3.5	−2.4	4.7	−0.7	1.1
8–9	26	0.4	4.4	−0.9	6.6	−1.3	8.3	−0.5	1.1
9–10	18	−1.2	2.2	−2.9	4.2	−2.8	5.4	−0.5	0.8
10–11	11	0.4	1.7	−1.1	3.8	−3.5	5.9	−1.1	1.3
				48-km FOV					
0–1	21 890	0.2	0.7	0.7	1.5	1.5	3.5	0.4	0.7
1–2	1749	0.9	1.7	2.0	3.5	4.6	7.3	0.6	1.1
2–3	526	1.2	2.4	2.1	3.9	4.1	6.9	0.4	1.0
3–4	217	1.7	3.1	2.5	5.1	4.3	8.2	0.3	1.0
4–5	102	0.8	2.6	0.8	4.0	1.7	6.1	0.0	0.8
5–6	43	0.9	2.4	0.8	3.3	1.9	5.3	−0.1	0.9
6–7	28	1.4	4.5	1.1	5.8	3.3	8.9	0.2	1.3
7–8	16	1.5	3.2	0.8	3.7	1.0	5.7	0.2	0.7
8–9	10	2.7	3.0	2.1	2.8	2.4	3.9	0.1	0.3

contribution to the uncertainty is due to the uncertainty in the rainfall inhomogeneity itself. Uncertainty added to the retrieval problem by radiative transfer requirements, however, is not negligible.

5. Summary and conclusions

The intention of this paper was to begin focusing attention on error models for passive microwave rainfall algorithms. To that end, the sources of uncertainty related to rainfall inhomogeneity were examined in detail, and it was shown how these could be used to establish realistic error models. The work, however, is far from finished. Based upon the results presented here, it is clear that much of the uncertainty associated with individual satellite FOVs is due to the uncertainty in the rainfall inhomogeneity itself. Before results can be trusted, the rainfall statistics derived here need to be enhanced significantly. Rainfall data with 2-km resolution will be available from the TRMM ground validation program for numerous sites around the Tropics beginning in late 1997. Other radar data from around the globe can further add to knowledge of the bias component of the inhomogeneity for global applications. With only three IOPs available from the TOGA COARE data, it is especially this bias component that needs to be better quantified if accurate uncertainties are to be determined.

Section 3 of this paper examined some general assumptions needed to treat inhomogeneous rainfall in a forward model. It was found that the gamma distribution much better represented the explicitly computed Tb than a lognormal distribution. For the purposes of the example, only the gamma distribution was therefore considered. The two distributions considered here, however,

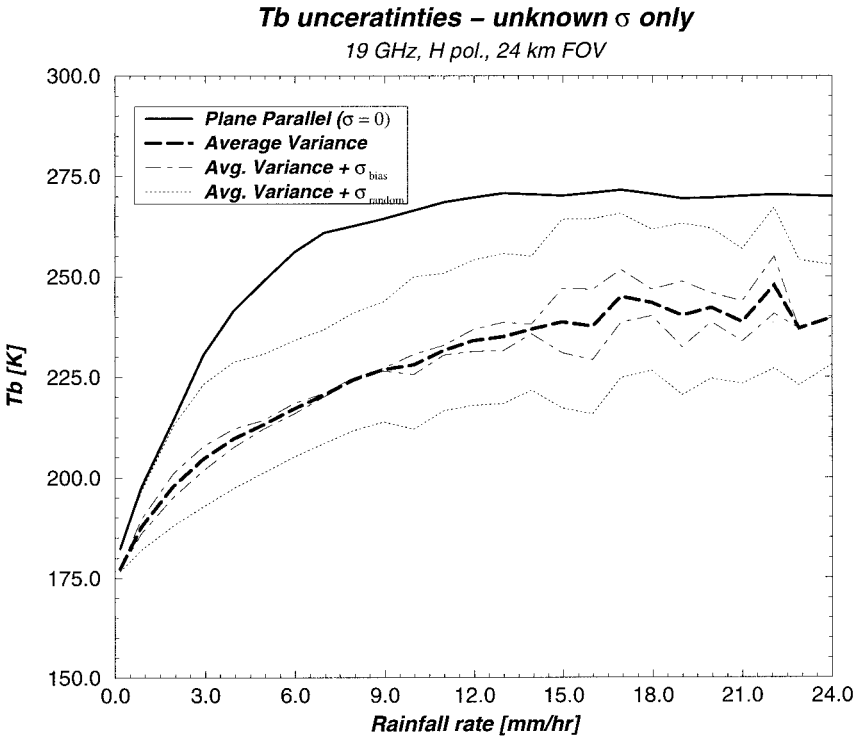

FIG. 9. Error model for 19-GHz, horizontally polarized radiation. Uncertainties shown are due to uncertainties in rainfall inhomogeneity only. No subsequent errors due to radiative approximations are assumed.

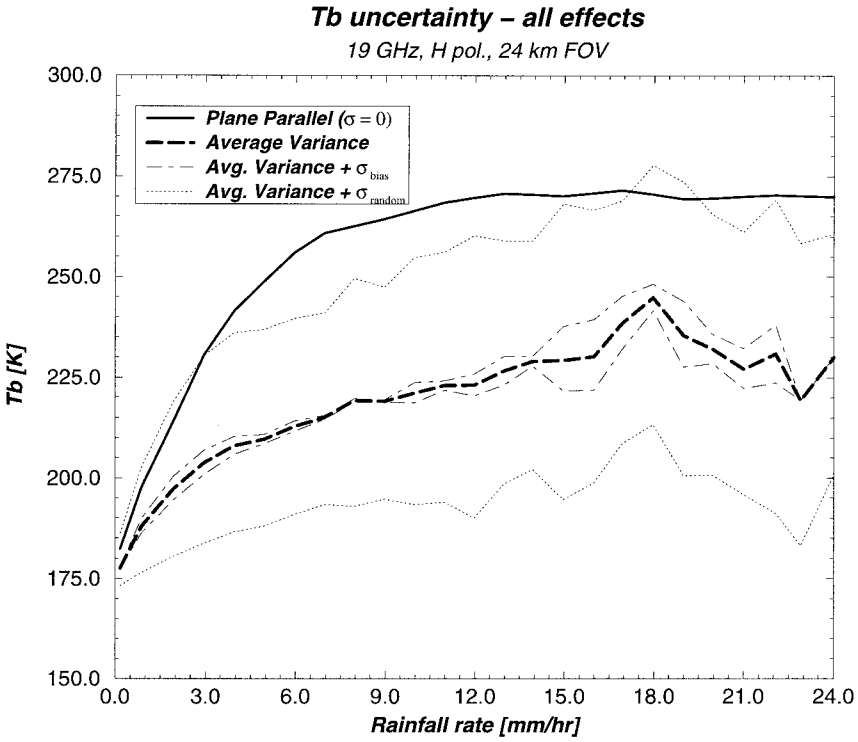

FIG. 10. Error model for 19-GHz, horizontally polarized radiation. All errors, including uncertainties in rainfall inhomogeneity as well as radiative approximations, are shown.

do not constitute all possible choices. It may well be that other distributions can better capture the explicit Tb. Random errors could be decreased if such a distribution were found. The bias errors associated with the three-dimensional radiative transfer were found to be quite small. The same cannot be said for the random error component. Particularly as satellite FOVs become smaller, this source of random error is significant. Finally, it should be said that the error model for going from an explicit distribution to the rainfall that can be simulated was done in two separate steps. The first step considered the errors associated with describing the rainfall by a statistical distribution, while the second considered the errors due to three-dimensional radiative effects. With some increased computer resources, these two steps can be combined. This would eliminate the need to assume that the two effects are uncorrelated and would make for a more elegant framework.

The error model discussed here focused only on error estimates based upon rainfall statistics and broad assumptions needed to compute Tb for inhomogeneous fields. Once such an error model is in place, however, it follows that improvements can be made in algorithm assumptions that will reduce both the bias and random error components. Using additional Tb's or texture information to classify rainfall, for instance, might lead to radar statistics, which are more uniform within each category. If the probability of correctly classifying each type of precipitation is high enough, such a scheme may well reduce the overall error sources. Using a multiple channel Tb might likewise help reduce the errors if the channels can be selected so as to minimize the effect of inhomogeneity. Once an error model is in place, these assumptions can all be rigorously tested.

Finally, it must be said that while the horizontal inhomogeneity is perhaps the greatest single source of error in retrieval algorithms, it is not the only source. Other components such as the vertical structure and background fields need to be examined. If rainfall inhomogeneity is considered as the only source of error, then the proper conclusion from this paper would be that the 85-GHz channel is best suited for rainfall retrievals because the linearity in the Tb to rainfall relations makes it rather insensitive to changes in rainfall statistics. The 85-GHz channel, however, suffers from large uncertainties between integrated ice content and surface rainfall. Certain areas of the world, which contain little or no ice in precipitating clouds, will lead to large regional differences, which in turn will lead to large bias errors, as defined in section 1. The uncertainty in 85-GHz-based retrievals should, in fact, be dominated by the uncertainty in the ice concentration to rainfall relations. This paper did not address the uncertainties in the vertical structure. Using cloud model structures, such as the GCE model described earlier, is one possibility to get statistics regarding the different vertical structures that are possible for a given rainfall. Another possibility may lie in the analysis of dual-polarization radar data that can distinguish certain particle habitats. The work done here represents an initial step. Much work still needs to be done before satisfactory error models can be constructed. By breaking it up into component pieces, however, such a task is perhaps less daunting.

Acknowledgments. The author would like to thank Dr. David Short for his help and many discussions on error modeling, as well as the three anonymous reviewers for their helpful suggestions. This work was supported by Drs. Ramesh Kakar and Gassem Asrar of NASA Headquarters as part of the prelaunch TRMM and EOS-AMSR algorithm development efforts.

REFERENCES

Bell, T. L., 1987: A space-time stochastic model of rainfall for satellite remote sensing studies. *J. Geophys. Res.,* **92,** 9631–9643.

——, A. Abdullah, R. L. Martin, and G. R. North, 1990: Sampling errors for satellite-derived tropical rainfall: Monte Carlo study using a space-time stochastic model. *J. Geophys. Res.,* **95,** 2195–2206.

Chiu, L. S., G. R. North, D. A. Short, and A. McConnell, 1990: Rain estimates from satellite: Effect of the finite field of view. *J. Geophys. Res.,* **95,** 2177–2185.

Kozu, T., and T. Iguchi, 1996: A preliminary study of non-uniform beam filling correction for spaceborne radar rainfall measurement. *IEICE Trans. Commun.,* **E79–B,** 763–769.

Lin, Y.-L., R. D. Farley, and H. D. Orville, 1983: Bulk parameterization of the snow field in a cloud model. *J. Climate Appl. Meteor.,* **22,** 1065–1092.

Liu, Q., C. Simmer, and E. Ruprecht, 1996: Three-dimensional radiative effects of clouds in the microwave spectral range. *J. Geophys. Res.,* **101,** 4289–4298.

North, G. R., S. S. P. Shen, and R. Upson, 1993: Sampling errors in rainfall estimates by multiple satellites. *J. Appl. Meteor.,* **32,** 399–410.

Petty, G., 1994: Physical retrievals of over-ocean rain rate from multichannel microwave imagery. Part I: Theoretical characteristics of normalized polarization and scattering indices. *Meteor. Atmos. Phys.,* **54,** 79–99.

Roberti, L., J. Haferman, and C. Kummerow, 1994: Microwave radiative transfer through horizontally inhomogeneous precipitating clouds. *J. Geophys. Res.,* **99,** 16 707–16 718.

Short, D. A., and G. R. North, 1990: The beam filling error in *Nimbus-5* electronically scanning microwave radiometer observations of Global Atlantic Tropical Experiment rainfall. *J. Geophys. Res.,* **95,** 2187–2193.

——, P. A. Kucera, B. S. Ferrier, and O. W. Thiele, 1995: COARE IOP rainfall from shipborne radars: 1. Rain mapping algorithms. *Proc. 27th Conf. on Radar Meteorology,* Vail, CO, Amer. Meteor. Soc., 678–680.

Simpson, J., C. Kummerow, W. K. Tao, and R. F. Adler, 1996: On the Tropical Rainfall Measuring Mission (TRMM). *Meteor. Atmos Phys.,* **60,** 19–36.

Soong, S.-T., and Y. Ogura, 1973: A comparison between axisymmetric and slab symmetric cumulus models. *J. Atmos. Sci.,* **30,** 879–893.

Tao, W.-K., and S.-T. Soong, 1986: A study of the response of deep tropical clouds to mesoscale processes: Three-dimensional numerical experiments. *J. Atmos. Sci.,* **43,** 2653–2676.

——, and J. Simpson, 1993: Goddard Cumulus Ensemble model. Part I: Model description. *TAO,* **4,** 35–72.

Wilheit, T. T., A. T. C. Chang, M. S. V. Rao, E. B. Rodgers, and J. S. Theon, 1977: A satellite technique for quantitatively mapping rainfall rates over the oceans. *J. Appl. Meteor.,* **16,** 551–560.